



Transition from vortex-induced vibrations to galloping in a flexible square prism

Bridget M. Benner¹ , Adrian G. Carleton¹  and Yahya Modarres-Sadeghi¹ 

¹Department of Mechanical and Industrial Engineering, University of Massachusetts, Amherst, MA 01003, USA

Corresponding author: Yahya Modarres-Sadeghi, modarres@engin.umass.edu

(Received 23 March 2024; revised 15 January 2025; accepted 16 January 2025)

We study the response of a flexible prism with a square cross-section placed in cross-flow through a series of experiments conducted at increasing flow velocities. We show that as the reduced velocity (a dimensionless flow velocity that also depends on the natural frequency of the structure) is increased, the prism undergoes vortex-induced vibration (VIV) in its first mode, which then transitions to VIV in the second mode and then third mode. In these ranges, the shedding frequency is synchronised with the oscillation frequency, and the oscillations are mainly in the transverse (cross-flow – CF) direction. As we keep increasing the reduced velocity, we observe a linear increase in the amplitude of the torsional oscillations of the prism, resembling a torsional galloping. This increase in the torsional oscillations then causes an increase in the amplitudes of the CF and inline (IL) oscillations while the third structural mode is still excited in the CF direction. A transition to oscillations in the fourth structural mode is observed at higher reduced velocities, which reduces the CF and IL amplitudes, while the torsional oscillations reach a plateau. After this plateau is reached in the torsional oscillations, galloping is observed in the CF oscillations of the response, which results in large-amplitude oscillations in both the CF and IL directions. The CF galloping response at these higher reduced velocities is accompanied by a torsional VIV response and the shedding frequency is synchronised with the frequency of the torsional oscillations.

Key words: flow–structure interactions, vortex dynamics, vortex shedding

1. Introduction

We study the response of a flexible prism with a square cross-section that is placed perpendicular to an incoming flow. It is expected that this prism will undergo flow-induced oscillations, and here we study how these flow-induced oscillations depend on

© The Author(s), 2025. Published by Cambridge University Press. This is an Open Access article, distributed under the terms of the Creative Commons Attribution licence (<https://creativecommons.org/licenses/by/4.0/>), which permits unrestricted re-use, distribution and reproduction, provided the original article is properly cited.

the incoming flow velocity. Two types of flow-induced oscillations that are extensively observed when a bluff body is placed in flow are vortex-induced vibration (VIV) and galloping (Blevins 1990; Païdoussis *et al.* 2010; Modarres-Sadeghi 2022).

VIV is observed in a flexibly mounted bluff body when the frequency of vortex shedding in its wake equals the system's natural frequency. When the structure starts oscillating, its oscillation results in shedding of vortices in its wake at a frequency equal to the oscillation frequency and, therefore, deviating from the expected shedding frequency of a fixed bluff body as predicted by the Strouhal law. The range where the shedding frequency and oscillation frequency are equal is called the lock-in range and the oscillations that are observed within the lock-in range are called VIV.

VIV has been extensively studied for a cylinder placed in flow, especially when the cylinder is allowed to oscillate in a direction perpendicular to the direction of incoming flow, referred to as the transverse or cross-flow (CF) direction (Williamson & Govardhan 2004; Sarpkaya 2004). In this case, a lock-in range is observed over a range of reduced velocities, defined as $U^* = U/(f_{nw} D)$, where U is the incoming flow velocity, f_{nw} is the system's natural frequency in an otherwise still fluid and D is the cylinder's diameter. The lock-in range starts at a reduced velocity of approximately $U^* = 5$. The width of the lock-in range and the maximum amplitude of oscillations observed in the response depend on the system's mass ratio and the structural damping. This amplitude stays within approximately one cylinder diameter in the CF VIV cases.

If the degree of freedom is in line with the direction of the incoming flow, the observed oscillations are referred to as inline (IL) VIV (Cagney & Balabani 2014; Gurian, Currier & Modarres-Sadeghi 2019). In this case, two lock-in ranges are observed. The first lock-in range starts at a reduced velocity of approximately $U^* = 1.7$, where oscillations are rather unexpected. These oscillations only occur if a disturbance is given to the cylinder, as a result of which symmetric and alternating symmetric vortices are shed in the wake of the cylinder. The second lock-in range is observed for reduced velocities starting at approximately $U^* = 2.5$, which is the expected onset of lock-in for an IL VIV case (since the shedding frequency in the IL direction is twice that in the CF direction and, therefore, synchronisation is expected to occur at a reduced velocity half of that observed in CF VIV) and asymmetric vortex shedding is observed in the wake. The amplitudes of oscillations in the IL VIV cases are much smaller than those in the CF VIV cases and stay within 0.1 cylinder diameters in both ranges of oscillations.

When a cylinder is allowed to oscillate in both the CF and IL directions, oscillations are observed at larger amplitudes compared with their corresponding one degree of freedom (DOF) systems (Jauvtis & Williamson 2004; Dahl, Hover & Triantafyllou 2006, 2007, 2010). The response then depends on the ratio of the natural frequencies in the CF and IL directions. When a 1:2 ratio is observed (i.e. when the natural frequency in the IL direction is twice that in the CF direction), dual resonance is observed (Dahl *et al.* 2010) in which case the cylinder's oscillations are synchronised with the vortex-shedding frequency in both the CF and IL directions. In general, when large-amplitude 2DOF VIV responses are observed, the cylinder follows a so-called counterclockwise (CCW) figure-eight trajectory. On a CCW trajectory, the cylinder moves upstream when it is at the extremes of its CF path. Such oscillations are also accompanied by large third harmonic frequencies in CF forces.

When a flexible beam with a circular cross-section is placed perpendicular to the incoming flow, it undergoes VIV as well (Chaplin *et al.* 2005; Trim *et al.* 2005; Huera-Huarte & Bearman 2009; Bourguet *et al.* 2011b; Seyed-Aghazadeh, Edraki & Modarres-Sadeghi 2019). In these cases, as the reduced velocity is increased, the shedding

frequency synchronises with different natural frequencies of the structure and, therefore, different modes of the structure can be excited. Cases where two or more modes of the structure are excited at the same time have been observed as well. Since a flexible beam is free to oscillate in both the CF and IL directions, the trajectories that each cross-section of the beam follows during its VIV response are crescent or figure-eight trajectories, similar to what a 2DOF VIV system would do. It has been shown previously (Bourguet *et al.* 2011b) that the structure locally follows a CCW figure-eight trajectory when power is being transferred from the fluid to that region of the structure. Travelling waves then are observed in the beam's response that travel from the energy input regions towards the dampening regions. The trajectory of the beam could be CW or CCW within these dampening regions. There are several studies that consider flow-induced vibration of flexible structures placed in flow as summarised in recent reviews by Wu, Ge & Hong (2012); Ma *et al.* (2022) and Huera-Huarte (2024).

When instead of a cylinder, a bluff body with a non-circular cross-section is placed in flow, in addition to VIV, galloping can be observed as well. This is extensively studied for systems with 1DOF in the transverse direction and with square or triangular cross-sections (e.g. Nemes *et al.* (2012); Zhao *et al.* (2014); Seyed-Aghazadeh, Carlson & Modarres-Sadeghi (2017)). Zhao *et al.* (2010) and Nemes *et al.* (2012) studied the response of a flexibly mounted square prism allowed to oscillate in the CF direction and placed in flow at different angles of attack. They observed that a square prism undergoes a galloping response for smaller angles of attack (when zero corresponds to the angle at which a side of the square is perpendicular to the direction of flow), up to $\alpha = 7.5^\circ$. For slightly larger angles of attack in the range of $\alpha = 7.5^\circ - 10^\circ$, they observed VIV at lower reduced velocities and galloping at higher reduced velocities. They showed that the response transitions to mainly VIV for even higher angles of attack, with no galloping observed at higher reduced velocities. We recently studied the response of a flexibly mounted square prism when it is free both in the CF and the IL directions to investigate the influence of the extra degree of freedom in the IL direction on the system's behaviour (Carlson, Currier & Modarres-Sadeghi 2021). We observed a VIV response at higher angles of attack, $\alpha = 20^\circ - 45^\circ$, where the sharp edge of the prism saw the incoming flow first. As the angle of attack was decreased, we observed that a galloping response started to develop at higher reduced velocities for angles of attack within the range of $\alpha = 10^\circ - 15^\circ$. For the smallest angles of attack, $\alpha = 0^\circ - 5^\circ$, we observed VIV at lower reduced velocities and galloping at higher reduced velocities. For these angles of attack, the oscillations persisted for the entire range of reduced velocities tested, after the initial VIV response was observed. For the cases where the galloping response was observed at higher reduced velocities, the prism followed very complicated four-lobe trajectories.

In the present work, we focus on a case where a flexible beam with a square cross-section is placed perpendicular to the incoming flow, such that at zero flow velocity, its side sees the flow first. This is the configuration that, for a 2DOF system, we observed a transition to galloping in the response. By considering a flexible structure, in addition to the two degrees of freedom in the CF and IL directions at each cross-section of the beam, we also have the degree of freedom in the torsional direction. Again, since this is a flexible beam, its different modes could be excited due to its interactions with the incoming flow. Here, we show the results of our experiments as we increased the incoming flow velocity and observed the response of a flexible beam with a square cross-section and its wake.

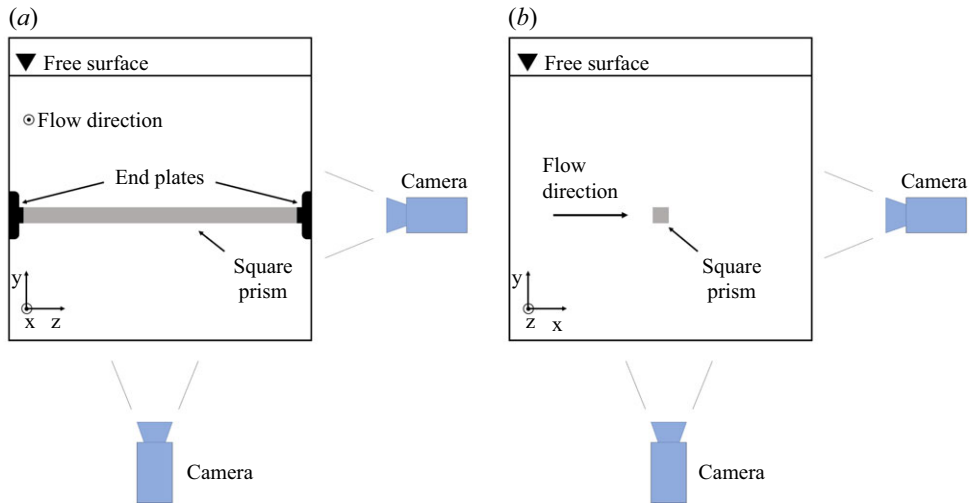


Figure 1. Schematic of the experimental set-up in (a) the downstream view and (b) the side view.

2. Experimental set-up and measurement techniques

2.1. Experimental set-up

The experiments were conducted in a re-circulating water tunnel, with a test section of $1.27 \text{ m} \times 0.5 \text{ m} \times 0.38 \text{ m}$ and a turbulence intensity of less than 1% for a flow velocity of up to $U = 0.3 \text{ m s}^{-1}$. A flexible square prism made of silicone rubber with a side length of $D = 9.5 \text{ mm}$ and length of $L = 34.5 \text{ cm}$, for an aspect ratio of $L/D = 36.2$, was placed horizontally in the test section of the water tunnel. The corner radius of the prism was 2% of the side length. To support the structure, we used three-dimensional (3-D) printed (nylon-11) mounting plates on either side of the water tunnel and magnets to secure the mounting plates to the sides of the test section, as shown in figure 1. The prism was stretched when mounted in the water tunnel to a stretched length of $L_s = 35.8 \text{ cm}$ and, as such, was under tension. The structure was placed at an angle of attack of $\alpha = 0^\circ$, such that the flat side of the square cross-section was the first to see the incoming flow. The natural frequency of the square prism in otherwise still water was determined to be $f_{nw} = 3.9 \text{ Hz}$ and in air, $f_{na} = 5.9 \text{ Hz}$. The natural frequency was determined by taking the fast Fourier transform (FFT) of a decay test whereby an initial displacement was provided in still water and in air, and the response of the system was recorded over a period of time. We also conducted a decay test for the torsional response of the prism in water and used the resulting time history to calculate the torsional natural frequency of $f_{tw} = 15 \text{ Hz}$, or $3.8 f_{nw}$. The mass ratio was determined to be $m^* = 1.23$. The damping ratio was determined, using a decay test and exciting the structure in the first mode, to be $\zeta = 0.0098$. The mass ratio, m^* , the damping ratio, ζ , and the reduced velocity, U^* , are the dimensionless parameters that define this system. If one has a different experiment but matches these dimensionless parameters, the response (as a function of parameter U^*) would be the same as what we have observed here. The tension that was applied to the beam was $T \approx 1.0 \text{ N}$, Young's modulus, calculated by loading the prism in tension using an ATI Nano-17 6-axis force sensor and tracking the elongation with a Micro-Epsilon optoNCDT ILD1402 laser, was $E \approx 290 \text{ kPa}$ and the structure's length was $L = 345 \text{ mm}$, which resulted in a value of $R = n^2 \pi^2 EI / (L^2 T) = 0.017$ for the ratio between the flexural-rigidity-dominated and tension-dominated terms in

calculating the system's natural frequency for $n = 1$. As a result, we confirm that the beam is tension dominated. The effect of the flexibility of the structure as well as the externally applied tension are reflected in the reduced velocity, $U^* = U/(f_{nw}D)$. In this definition, f_{nw} , the natural frequency of the structure in otherwise still fluid, is related to the flexural rigidity of the structure as well as the externally applied tension, $f_{nw} = \sqrt{(n^4\pi^2)/(4L^2))(EI/(\rho A)(1 + C_M)) + (n^2/(4L^2))(T/(\rho A)(1 + C_M))}$, where C_M is the added mass coefficient (Modarres-Sadeghi 2022). As the beam is tension dominated, only variation of the external tension can influence the natural frequency. In many previous studies on VIV of flexible structures, the system has been tension dominated.

2.2. Displacement and flow visualisation tests

Two cameras, a Phantom Miro M110 high-speed camera and a Chronos 1.4 high-speed camera, were used to capture the response of the flexible square prism in the cross-flow and inline directions. An in-house MATLAB code was then used to track the response of each pixel along the edges and across the length of the structure. This allowed us to capture the motion of the structure to a degree that is only limited by the resolution of the camera, effectively giving us a continuous measurement along the structure's length. This method decreases data analysis time and improves measurement accuracy over the method of response reconstruction from discrete point measurements previously used in the study of flexible structures undergoing VIV (e.g. by Seyed-Aghazadeh *et al.* (2017)). The displacement measurement technique that we have used here is an extension to the method we used a while ago in a series of experiments on VIV of flexible structures placed in flow (Seyed-Aghazadeh & Modarres-Sadeghi 2016; Seyed-Aghazadeh *et al.* 2019, 2021). In those tests, we tracked a series of markers that we had painted along the length of the flexible structure – approximately 10–15 points – and then used different interpolation techniques to obtain a continuous representation of the response of the flexible structure based on the information obtained from these limited tracked points. In our measurement in the present work, instead of marking some points on the structure to track, we track all the pixels at the edge of the structure. This means that instead of tracking only 10–15 points, we track over 1000 points along the length. Since we have many more points in the current version, we can present the response of the structure continuously without any need for interpolation. The error of the measurement method is of the order of 2–3 % of the structure's side, i.e. $0.02D$. The amplitudes that we have measured here are much larger than $0.02D$ and, therefore, the measurement error does not influence our conclusions. For example, amplitude error bars shown later in figure 4 would have been of a size comparable with the symbol sizes we have used in the plot.

The displacement of the square prism was recorded over a duration of ~ 15 s, once the structure reached steady state, at each flow velocity. Tests were conducted over a range of reduced velocities, $1.4 < U^* < 14.2$, corresponding to a Reynolds number range of $500 < Re < 5100$. For all experiments, the water level was held constant and flow was increased in increments of 5 mm s^{-1} to cover the reduced velocity range tested. To calculate the magnitude of the torsion in the structure, θ , the footage from the downstream camera was used to measure the apparent thickness of the structure in the recording, h , which is the result of the prism's rotation. The rotation can then be calculated for the range $-45^\circ < \theta < 45^\circ$ as

$$\theta = \sin^{-1}(h/\sqrt{2}D) - 45^\circ. \quad (2.1)$$

The measuring accuracy was within 1 pixel, whereby 1 pixel ~ 0.3 mm and 1.6° . The torsion time histories were smoothed using the default smooth function in MATLAB with a moving average window size of 5. The cameras used to track the IL and CF displacement were synchronised using a trigger switch cable that was connected to both cameras. The third camera was used for flow visualisation and was not synchronised with the IL and CF displacements. Discrete points were not drawn on the structure to track the displacement. Instead, we used an in-house MATLAB code that located the edges of the prism for each frame, and quantified the displacement and torsion along the length of the structure. The number of points depended on the size of the image, which changed slightly for each camera, but it was in the range of 1090–1150 points. The sampling frequency was 100 fps in the IL direction and the CF direction up to $U^* = 10.1$, and 500 fps in the CF direction for larger reduced velocities when the torsional response became significant. To support the structure, we used 3-D printed (nylon-11) mounting plates and used magnets to secure the mounting plates to the sides of the water tunnel.

To study the vortex shedding in the wake of the square prism, flow visualisation tests were conducted using hydrogen bubbles. A detailed description of the system used for hydrogen bubble generation is documented by Currier *et al.* (2021). Hydrogen bubbles were generated via electrolysis whereby a stainless steel wire was placed horizontally along the length of the square prism to capture the shedding patterns along the length of the structure and also vertically across the test section at varying points along the length of the square prism to obtain a more detailed view of the shedding patterns. The stainless steel wire served as an anode and a positively charged graphite plate served as a cathode. The potential between the two caused hydrogen bubbles to form along the wire. The bubbles then separated from the wire creating a bubble plane used to view the wake of the square prism. Images of the wake were captured using a Phantom Miro M110 high-speed camera. Additionally, particle image velocimetry (PIV) measurements were recorded at various flow velocities and locations along the length of the prism. For these recordings, the water tunnel was seeded with $50\ \mu\text{m}$ polyamid particles which were illuminated with 520-nm wavelength sheet lasers. The images were recorded using the same Phantom Miro M110 high-speed camera and the recordings were processed in the PIVlab MATLAB app (Stamhuis & Thielicke 2014).

3. An overall view of the response

First, we discuss the overall behaviour of the prism as the flow velocity, represented in the form of the reduced velocity, U^* , is increased. The normalised amplitude of oscillations in the CF direction, $A_{CF}^* = A_{CF}/D$, along the normalised length of the square prism, $z^* = z/L$, is shown in [figure 2](#). This plot is produced by assembling the root-mean-square (r.m.s.) values of the amplitude of oscillations at different reduced velocities and placing them next to each other. The normalised oscillation frequencies in the CF direction, $f_{CF}^* = f_{osc}/f_{nw}$, versus the reduced velocity, U^* , are shown in [figures 3\(a\)–3\(c\)](#) at three locations along the length of the prism ($z^* = 0.3, 0.4$ and 0.5) to show the frequencies that are observed at different reduced velocities. These plots are produced by placing the FFT plots of the displacement time histories at different reduced velocities next to each other in a 3-D plot. We show these frequencies at three different locations along the length of the structure, so that when different modes of the structure are excited, their frequencies would be reflected in these plots. In addition to the frequency of the structure's oscillations, frequency of shedding observed in the wake of the prism is plotted at sample reduced velocities in [figures 3\(d\)–3\(h\)](#). These plots are made using the wake vorticity plots that are calculated based on the PIV results for over 2000 frames. We calculate the FFT of

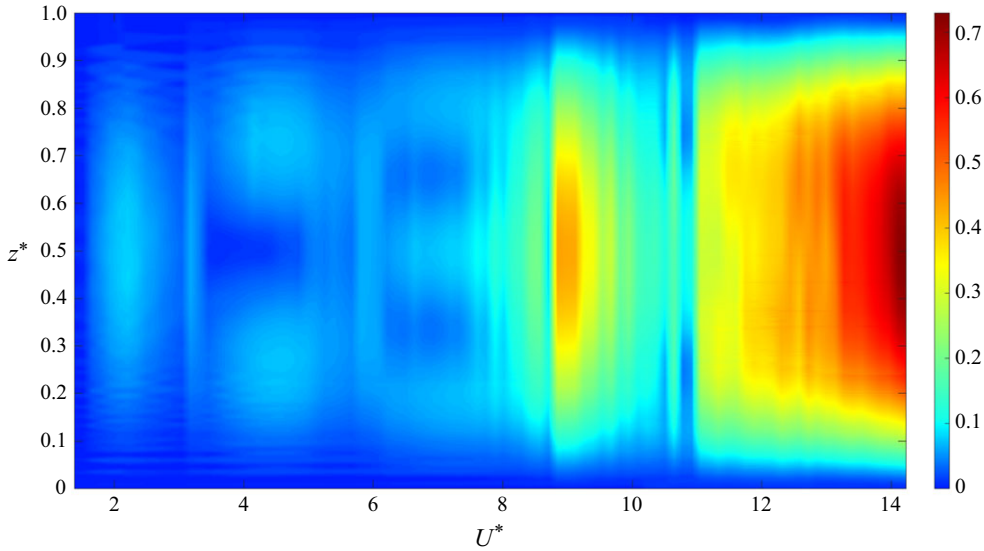


Figure 2. Amplitude of oscillations in the cross-flow direction, A^* (colour), along the prism's length, z^* , versus the reduced velocity, U^* .

the vorticity over time for all the points along the height ($y^* = y/D$) of each frame at approximately $1.5D$ downstream from the structure and place all these FFT plots next to each other to create the 3-D plots of the figure.

3.1. VIV of the first, second and third structural modes

The amplitude plot of figure 2 shows that the prism oscillates at its first structural mode for low reduced velocities. This is clear in the plot as a mainly first-structural-mode response with a maximum at its centre for $U^* < 3$. This primarily first-mode oscillation is also clear in the frequency plots of figure 3, where for all three points shown in the figure, a peak frequency at $f_{CF}^* \approx 1$ is observed. This frequency increases slightly as the reduced velocity is increased, similar to what has been observed extensively within the lock-in range of the VIV response of a 1DOF system placed in water (Williamson & Govardhan 2004). The sample shedding frequency within this region, i.e. $U^* = 2.2$ in figure 3(d), shows two peaks at $f_{vs}^* \approx 1$ on the two sides of the cross-section, which confirms that vortices are shed at the same frequency as the oscillation frequency, and therefore synchronisation between the structure and the vortex shedding is observed. Two peaks that are observed in the vortex shedding frequency plot (at $y^* \approx +1$ and -1), correspond to the two vortices that are shed from the two sides of the prism.

At a reduced velocity of approximately $U^* = 3$, the oscillations transition to the second structural mode. In the amplitude plot of figure 2, this is observed in the form of a low-amplitude response at approximately $z^* = 0.5$ and two peaks at approximately $z^* = 0.25$ and $z^* = 0.75$ for a range of reduced velocities of $3 < U^* < 6$. For this range, the frequency plots of figure 3 show a peak that increases with increasing velocity from $f_{CF}^* \approx 2$ to $f_{CF}^* \approx 2.5$ at $z^* = 0.3$ and 0.4 . As expected from a mainly second-structural-mode response, this frequency peak is not observed at $z^* = 0.5$, since this location corresponds to a node. The shedding frequency in figure 3(e) for $U^* = 4.7$ shows peaks of shedding frequency at $f_{vs}^* \approx 2.2$, which is the same as the oscillation frequency at this reduced velocity.

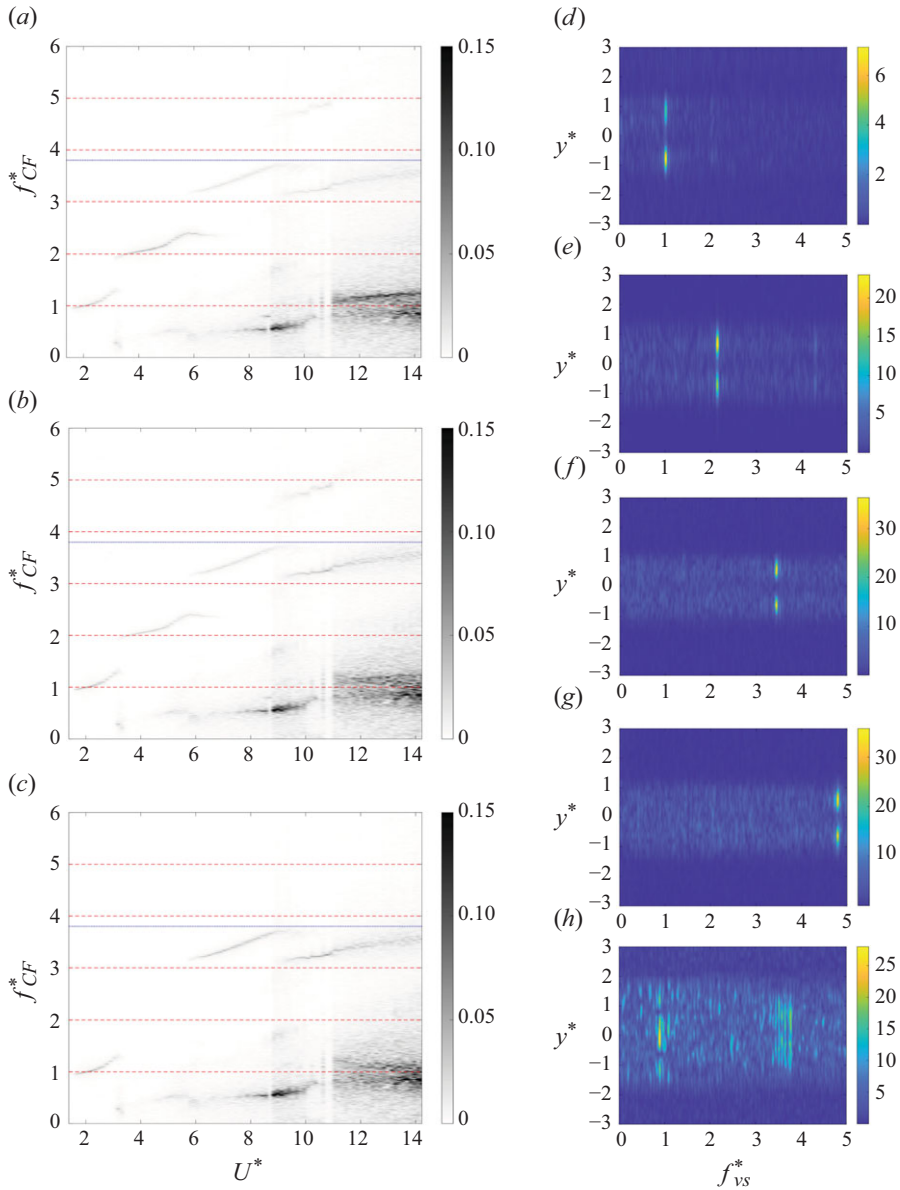


Figure 3. (a–c) Oscillation frequencies in the cross-flow direction versus the reduced velocity at points (a) $z^* = 0.3$, (b) $z^* = 0.4$ and (c) $z^* = 0.5$ along the length of the structure. The dashed red lines show the natural frequencies in the cross-flow direction and the dotted blue line shows the torsional natural frequency. (d–h) Vortex shedding frequencies, $f_{VS}^* = f_{VS}/f_{NW}$, versus a dimensionless distance in the cross-flow direction, $y^* = y/D$, for (d) $U^* = 2.2$ (at $z^* = 0.5$), (e) $U^* = 4.7$ (at $z^* = 0.25$), (f) $U^* = 7.7$ (at $z^* = 0.5$), (g) $U^* = 10.1$ (at $z^* = 0.4$) and (h) $U^* = 13.6$ (at $z^* = 0.5$).

For the range of reduced velocities of $6 < U^* < 8$, the third structural mode is excited, and a peak frequency beginning at $f_{CF}^* \approx 3$ is observed in figure 3 for this range, and the shedding frequency at the sample reduced velocity which is picked towards the end of this range (i.e. $U^* = 7.7$) corresponds to the oscillation frequency at this reduced velocity, confirming a synchronisation between the third-mode oscillations of the prism and the shedding of vortices in its wake.

3.2. Translational galloping

The response of the prism very clearly follows a different pattern for $U^* > 8$. Instead of excitation at higher structural modes, a strong contribution of the first structural mode is observed in the amplitude response of [figure 2](#) for this range of reduced velocities. The magnitude of this mainly first-structural-mode response increases sharply around $U^* = 9$, then it decreases over a range of reduced velocities, and again increases starting at approximately $U^* = 11$, and reaches a maximum of $A^* = 0.7$ at the centre of the beam for the maximum reduced velocity tested here. The frequency plots of [figure 3](#), however, show a contribution of the fourth mode (a line at $f_{CF}^* \approx 4.5$ in [figure 3b](#)), in addition to a large contribution of the first mode. The first-mode contribution shows up as a thick line towards the beginning of this reduced velocity range ($8 < U^* < 11$) and becomes a wide-spread contribution of frequencies at larger reduced velocities ($U^* > 11$). In addition to the fourth-mode frequency contribution that is only observed in [figure 3\(b\)](#) and the strong first-mode frequency contribution, another line is observed in the frequency plots of [figure 3](#) at $f_{CF}^* \approx 3$ for $U^* > 10$. We will discuss the source of this higher frequency later in [§ 4.4](#). For now, it is observed that there are ranges of reduced velocity, for example, $10 < U^* < 11$, for which we observe the large-amplitude first-mode excitation as well as the fourth-mode frequency excitation of the structure. The contribution of this fourth-mode excitation is clearly shown in the vortex shedding frequency plot of $U^* = 10.1$ in [figure 3\(g\)](#), which is picked from a very narrow range of reduced velocities over which the fourth mode becomes the major contributor to the response. As we will discuss later with some details, this first-mode response is a translational galloping response of the system and the fourth-mode response is a VIV response of the system. They co-exist over a range of reduced velocities, and then the translational galloping response, having the potential of assuming larger amplitudes compared with the fourth-mode VIV response, takes over and becomes the only response that is observed at higher reduced velocities, i.e. $U^* > 11$. We stopped the tests as the observed oscillations were close to causing damage to the experimental set-up. The amplitudes of the CF and IL oscillations reach values of $A_{CF}^* \approx 0.75$ and $A_{IL}^* \approx 0.6$ towards the end of the range shown here. These values for the IL amplitudes of oscillations are much larger in comparison with the typical magnitudes that are observed for the IL oscillations in the VIV response of flexible structures, which are typically at $A_{IL}^* \approx 0.2$ (Seyed-Aghazadeh & Modarres-Sadeghi 2016).

3.3. Torsional galloping

To further discuss the behaviour of the prism at larger reduced velocities, we plot the maximum amplitude of oscillations in the CF, IL and torsional directions versus the reduced velocity in [figure 4](#). By looking at these maximum values next to each other, it becomes clear that the sharp increase in the CF and IL response that is observed at approximately $U^* = 8$ corresponds to the beginning of the increase in the amplitude of torsional oscillations. At reduced velocities below this value, the magnitude of torsional oscillations stays below 4° . Starting from $U^* \approx 8$, the amplitude of torsional oscillations starts to increase linearly with increasing reduced velocity, suggesting that the structure is undergoing torsional galloping. The increase in the magnitude of torsional oscillations intensifies the oscillations in the CF and IL directions. At $U^* \approx 9$, the CF and IL amplitudes start to drop, while the amplitude of torsional oscillations keeps growing beyond this reduced velocity. This drop of the CF and IL oscillations is due to the transition from the third CF mode to the fourth CF mode within the reduced velocity range of $U^* = 8$ and $U^* = 11$. Once the mode switching from the third-mode CF VIV response

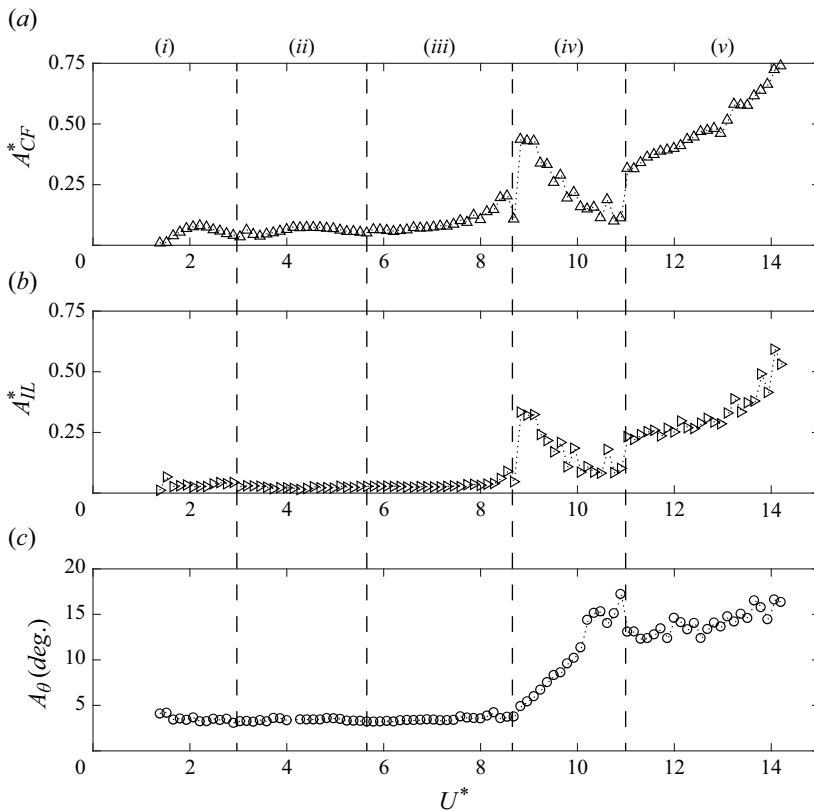


Figure 4. Maximum amplitude of the (a) CF, (b) IL and (c) torsional responses observed along the length of the structure versus the reduced velocity. The response is divided into five regions, indicated by the vertical dashed lines, that are characterised by (i) first-mode VIV, (ii) second-mode VIV, (iii) third-mode VIV, (iv) torsional galloping and (v) cross-flow galloping with torsional VIV.

to the fourth-mode CF VIV is finalised, by a reduced velocity of approximately $U^* = 11$, the amplitude of torsional response reaches a plateau at approximately 15° , while the amplitude of CF and IL displacements keep increasing with reduced velocity until the maximum reduced velocity tested here.

4. Detailed responses at sample cases

Here, we focus on five sample cases as the reduced velocity is increased to discuss the details of the prism behaviour during its different types of responses. Plots of r.m.s. amplitude versus length, amplitudes versus length and time, as well as the frequency contents versus length are given in [figure 5](#) for five distinctly different prism responses that shed light on the details of its response for increasing reduced velocities. Sample time histories of the CF displacement and their corresponding FFTs at the point of maximum amplitude of oscillations along the length of the prism for each of these five sample cases are shown in [figure 6](#). For the first four cases where VIV is observed, flow visualisations of the wake along the length of the prism are shown in [figure 7](#). The shedding frequency in the wake for these sample cases is given in [figure 3](#), and samples of side-view shedding in the form of PIV results in [figure 8](#).

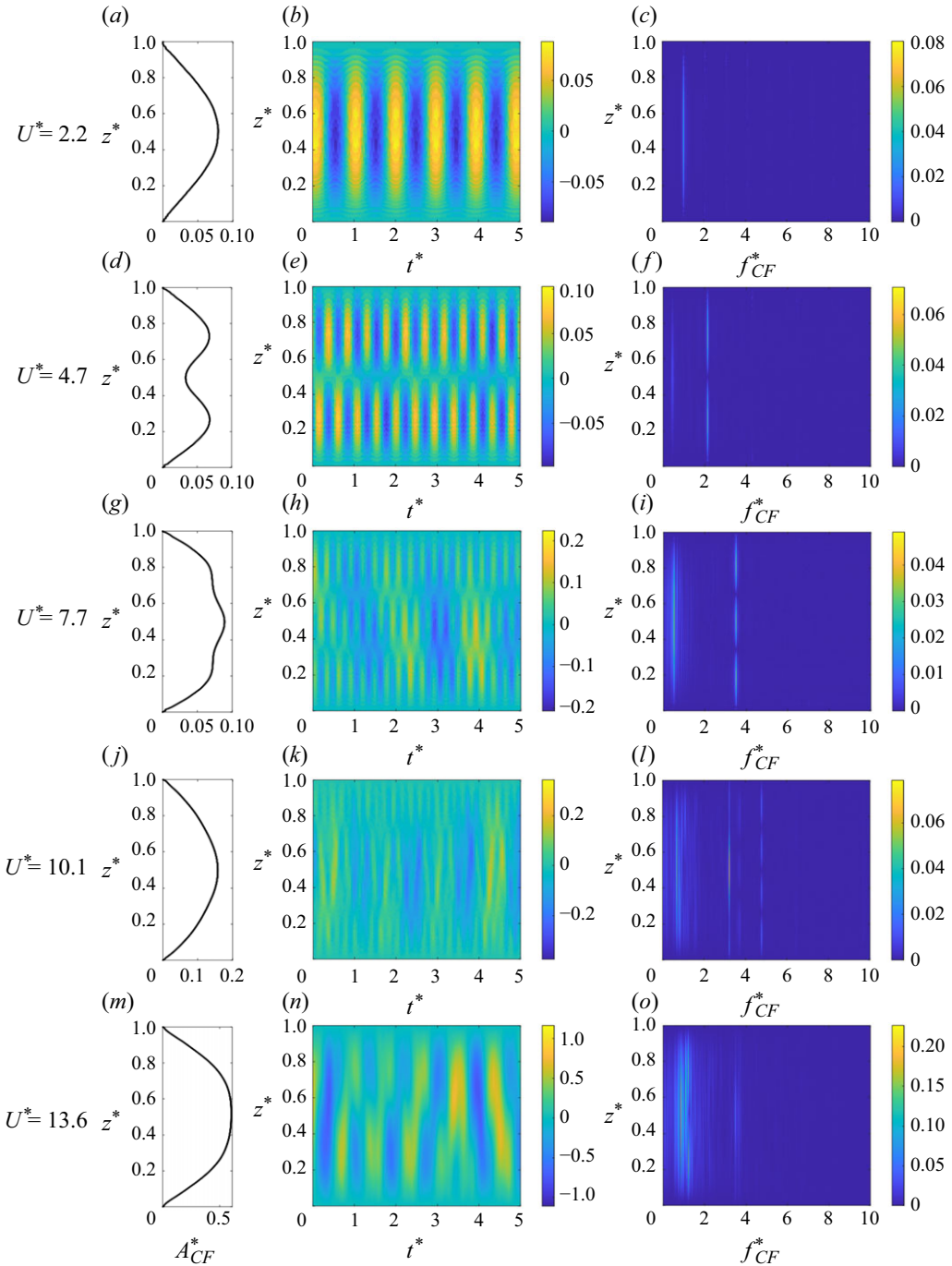


Figure 5. (a,d,g,j,m) Oscillation amplitudes, (b,e,h,k,n) time histories and (c,f,i,l,o) oscillation frequencies in the CF direction along the length of the square prism for $U^* = 2.2, 4.7, 7.7, 10.1$ and 13.6 .

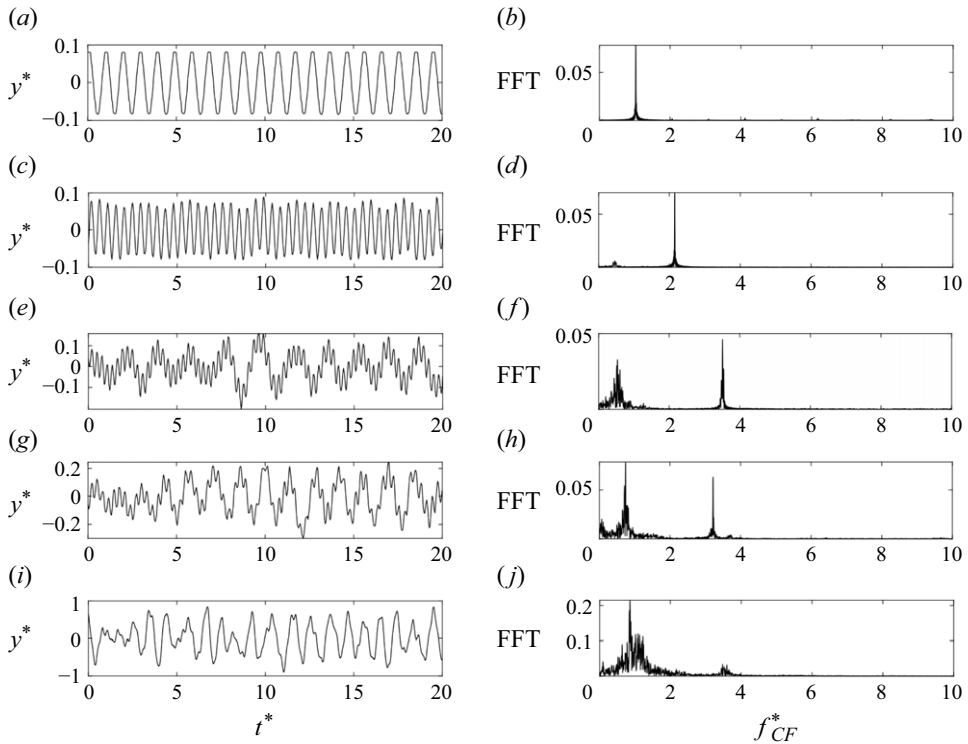


Figure 6. Time histories and their corresponding FFTs for the points along the length of the structure with the maximum amplitude of oscillations: (a,b) $U^* = 2.2$ at $z^* = 0.5$, (c,d) $U^* = 4.7$ at $z^* = 0.25$, (e,f) $U^* = 7.7$ at $z^* = 0.5$, (g,h) $U^* = 10.1$ at $z^* = 0.5$ and (i,j) $U^* = 13.6$ at $z^* = 0.5$, where $t^* = tf_{nw}$.

4.1. First-mode VIV – $U^* = 2.2$

The first sample case corresponds to a reduced velocity of $U^* = 2.2$, where a first-mode excitation is observed in the response of the prism. This response is clearly shown in figure 5(a,b,c), where a peak amplitude of $A_{CF}^* \approx 0.08$ is observed at approximately $z^* = 0.5$ over the entire time history that is shown in the figure. The response frequency stays at $f_{CF}^* \approx 1$, and the first-mode shape of the response is also clear in the frequency plot of this case. This single-peak response is also clear in the sample time history and its corresponding FFT plot in figure 6(a,b). It should be noted that in this case, the amplitude of oscillations in the CF direction is very small – only approximately $A_{CF}^* = 0.08$ – and no significant oscillations are observed in the IL direction, although clearly the degree of freedom does exist in that direction. The very small-amplitude oscillations in the CF direction, however, are enough to synchronise the shedding along the length of the prism, as seen in figure 7(a). Except for ranges close to the two side boundaries of the prism where no clear flow pattern is observed, vortices are shed synchronously along the length of the prism. The frequency of this shedding is equal to the oscillation frequency, as expected for a VIV case, as shown in the vortex shedding frequency plot of figure 3(d) and the vorticity plot of figure 8(a), and therefore synchronisation between the shedding and oscillation frequency has occurred and lock-in is observed, as expected for a VIV case.

4.2. Second-mode VIV – $U^* = 4.7$

At a slightly higher reduced velocity, $U^* = 4.7$, the second structural mode of the prism is excited, which can be clearly observed in the amplitude plots with two peaks at $z^* \approx 0.25$

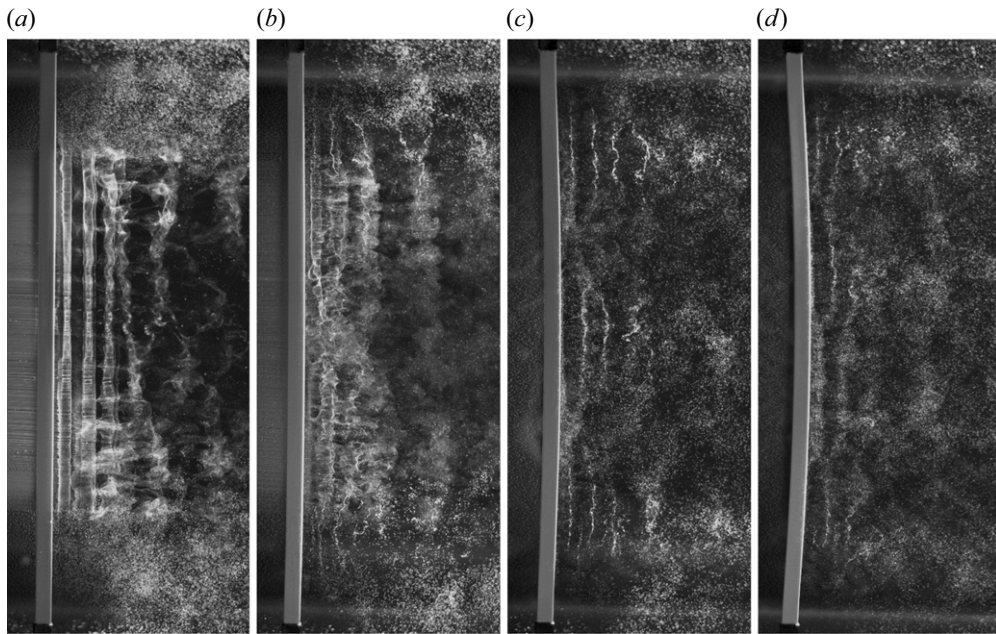


Figure 7. Wake of the square prism along its length as the structure undergoes VIV in its (a) first, (b) second, (c) third and (d) fourth modes, at the corresponding reduced velocities of $U^* = 2.2, 4.7, 7.7$ and 10.1 , respectively.

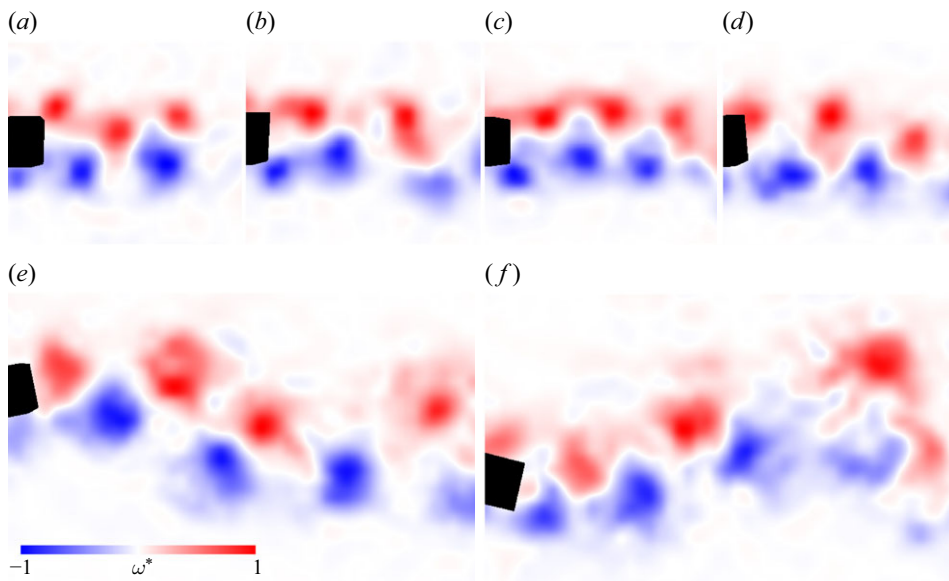


Figure 8. Normalised vorticity in the wake of the square prism at reduced velocities of (a) $U^* = 2.2$ at $z^* = 0.5$, (b) $U^* = 4.7$ at $z^* = 0.26$, (c) $U^* = 7.7$ at $z^* = 0.5$, (d) $U^* = 10.1$ at $z^* = 0.5$ and (e,f) $U^* = 13.6$ at $z^* = 0.5$ at two different time periods. The minimum and maximum vorticity values for each frame are (a) -37.9 and 41.7 , (b) -90.6 and 86.5 , (c) -119.1 and 127.1 , (d) -141.6 and 153.6 , (e) -164.1 and 183.3 and (f) -150.6 and 172.8 s^{-1} .

and $z^* \approx 0.75$, and a local minimum at $z^* \approx 0.5$ (figure 5d). The frequency plot of this case (figure 5f) also shows the two-peak response of the second mode that appears at a frequency approximately twice the first-mode frequency, i.e. $f_{CF}^* \approx 2$. Note that the local minimum at $z^* \approx 0.5$ does not correspond to a zero magnitude, which implies a travelling-wave-type response for the structure. The higher frequency response is also clear in the sample time history of figure 6(c,d). Also note the appearance of a very small frequency at approximately $f_{CF}^* = 0.5$. This is very small in this case, but will grow at higher reduced velocities, as we will see later. The second-mode response of the structure influences the shedding in its wake as seen in figure 7(b), where two rows of vortices are shed along the length of the structure – one on each side of the structure’s mid-point. The oscillations on each half of the structure cause synchronisation of vortex shedding along the range where oscillations are observed. The mid-point disrupts the shedding of vortices due to its minimal displacement. Similar to the first-mode response, the maximum observed amplitude is relatively small at approximately $A^* = 0.07$, and despite these small amplitudes, the oscillations do indeed synchronise the shedding in the wake. The vortex-shedding frequency measured in the wake (figure 3f) shows peaks at approximately $f_{vs}^* = 2$, similar to the peak observed in the oscillation frequencies, confirming the synchronisation between the structure and the fluid, and lock-in, at this mode as well. Similar to the previous case, the side view of the wake shown in figure 8(b) (this time at a cross-section located at $z^* \approx 0.25$) shows that two vortices are shed in each cycle of oscillations.

4.3. Third-mode VIV and the emergence of the galloping response – $U^* = 7.7$

At $U^* = 7.7$ (figure 5g,h,i), a third-structural-mode response of the flexible prism is observed with peak amplitudes at $z^* \approx 0.2$, 0.5 and 0.8 , and local minima at $z^* \approx 0.3$ and 0.7 . The third-structural-mode response of the prism is also observed in the frequency response of this case, with three bright bands at $f_{CF}^* \approx 3.5$. In addition to this frequency band, the frequency plot shows a single band at a frequency of $f_{CF}^* \approx 0.5$. This band did also exist very faintly in the frequency plot of the second-mode response, but in the present case, it is very clear, and it implies a first-structural-mode response (since it covers the entire length of the structure) at a low frequency of $f_{CF}^* \approx 0.5$. As a result, the amplitude response that is observed in this case is a combination of this low-frequency first-mode response and the higher-frequency third-mode response of the structure. Figure 9(a) shows the r.m.s. responses of the square prism constructed based on the contribution of the low-frequency galloping response only as well as its response constructed with the third-mode VIV response only. This plot is made by filtering the measured displacement around the respected frequencies of the first and third modes, and then calculating the r.m.s. values of the response. From this plot, it becomes clear that the magnitudes of the responses in these two modes are comparable: the first-mode galloping response reaches a magnitude of $A_{CF}^* \approx 0.075$ and the third-harmonic VIV response reaches a maximum peak of $A_{CF}^* \approx 0.05$. The contribution of the first-mode response in the total response is observed in bringing the local minima of the response to a non-zero point, since a pure first-mode response would not have had any node. Although the first-mode response has a magnitude comparable with the third-mode response, in the 3-D time histories of the response shown in figure 5(h), it is mainly the third-mode response that is observed. In this sense, the response is similar to that of the previous sample case, where the second-mode response was the main observed mode, despite the very faint contribution of the first-mode response. In the present case, the contribution of the first mode is much larger than in the previous case. This large contribution is clearly observed in the sample time

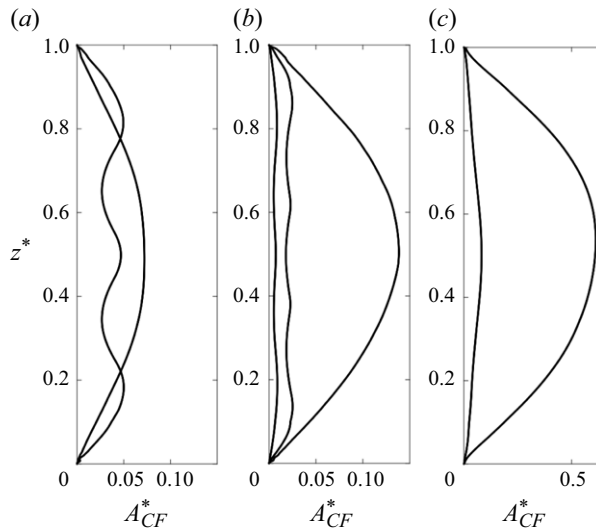


Figure 9. Amplitude of the structure along its length as a pure low-frequency galloping response and a pure high-frequency VIV response at (a) $U^* = 7.7$, (b) $U^* = 10.1$ and (c) $U^* = 13.6$.

history and FFT of [figure 6\(e,f\)](#), where a high-frequency response is superimposed on a low-frequency response. Without the higher frequency contribution, this response would have looked very much like a galloping response of the system. The amplitude of the total response at this reduced velocity is very similar to the amplitudes in previous cases with a maximum of $A^* \approx 0.09$ – only slightly larger than the previous case, but still much smaller than amplitudes observed typically in the VIV response of a structure with a circular cross-section.

Similar to the case of the second-mode excitation, in the present case, the local nodes of the response disrupt the shedding of vortices in the wake of the structure, as observed in [figure 7\(c\)](#). Three rows of vortices are shed in the wake of the structure. From the snapshot, it is clear that the vortex shedding patterns from the two side sections of the structure are synchronised with each other, while the shedding from the middle section is out of phase. This is a direct consequence of the structure's oscillation in its third mode, in which the two local maxima at the two side sections of the structure occur when the centre of the structure experiences its peak on the other extreme of the CF oscillations, and *vice versa*. The shedding frequency at this reduced velocity measured in the wake of the structure ([figure 3f](#)) has peaks at $f_{vs}^* \approx 3.5$, which is equal to the oscillation frequency at the third-mode response of the structure. This confirms the synchronisation between the structure and the vortex shedding, and therefore the third-mode contribution of the response is due to VIV at the third mode. The first-mode oscillations are a sign of galloping response, since it is a low-frequency response (lower than the expected, and observed, VIV response) and it is not synchronised with any shedding frequency in the wake of the structure. The snapshot of the wake shown in [figure 8\(c\)](#) shows that two vortices are shed in the wake in each cycle of oscillations.

In summary, at this reduced velocity, we observe mainly a VIV response, while a large contribution of a galloping response does exist. The overall response, however, looks like a VIV response, with the third-structural-mode oscillations and three rows of vortices shed in the wake corresponding to the third-beam-mode response of the structure. At higher reduced velocities, this behaviour changes.

4.4. *Co-existence of the VIV and the galloping responses* – $U^* = 10.1$

At a reduced velocity of $U^* = 10.1$ (figure 5j,k,l), the third-mode response that was observed in the previous sample case is replaced by a fourth-mode excitation at a normalised frequency of $f_{CF}^* \approx 5$. The first-mode response that was observed in the previous case, now has moved to a frequency of $f_{CF}^* \approx 1$, with a relatively wide band. A peak frequency is also observed at approximately $f_{CF}^* = 3$. The contribution of the fourth mode in the response is visible in the time history plots of figure 5(k), as a high-frequency response, and the low-frequency response shows up in the form of alternating blue and yellow regions. The r.m.s. amplitude plot (figure 5j) takes the form of pure first-mode oscillations, since the relative contribution of the VIV response (at the fourth mode) versus the galloping response (at the first mode) is decreased in comparison with the previous case. This is shown in the plots of figure 9(b), which correspond to the pure contributions of the first mode (galloping) and the third and fourth modes (VIV). The amplitude of the first-mode contribution is approximately six times that of the fourth-mode contribution (figure 9b). Compare this with the ratio of only approximately 1.7 for the amplitudes of the first- and third-mode contributions in the previous case where VIV was still the dominant response (figure 9a). Despite the dominance of the galloping response, even the small-amplitude fourth-mode excitation of the beam is enough to synchronise the vortices that are shed in the wake in the form of four distinct vortex rows, disconnected by the three nodes that are observed along the length of the structure (figure 7d). These vortices are shed at a frequency of approximately $f_{vs}^* = 5$, as seen in the wake measurements of figure 3(g). This frequency is the same as the normalised frequency of oscillations of the structure at its fourth mode as observed in figure 5(l). The sample time history and FFT plots of figure 6(g,h) are for the mid-point of the structure, and therefore only show the low-frequency large-amplitude oscillations. Naturally, the contributions of the fourth-mode response is not observed at this point on the structure. The shedding in the wake, as seen in figure 8(d), consists of two single vortices in each cycle of oscillations.

In summary, at this reduced velocity, we observe a co-existence of a galloping response that excites the first mode of the structure and a VIV response that excites the fourth mode of the structure. The galloping response has a much larger contribution in the total response in comparison with the previous sample reduced velocity, which results in an r.m.s. amplitude plot that resembles the first-mode response of the structure. The VIV response still influences the wake, and the vortices that are shed in the wake follow the VIV response frequency. This influence of the VIV response on the wake will not be observed at higher reduced velocities.

4.5. *Galloping prevails* – $U^* = 13.6$

At this reduced velocity (figure 5m,n,o), the only observed response is a low-frequency galloping response at the first mode of the structure. There is no sign of the high-frequency VIV response that we observed in the past two reduced velocities. The amplitude response along the length of the structure (figure 5m) is similar to the previous case – a first-mode response. The time history plot (figure 5n) shows travelling waves along the length of the beam, but only at the first mode, shown as switching blue and yellow colours in the figure. The contribution of the first-mode response in the total CF response is much larger at this reduced velocity in comparison with the lower reduced velocities (figure 9). The frequency plot (figure 5o) also exhibits one small peak at $f_{CF}^* \approx 1$, and a higher frequency at $f_{CF}^* \approx 4$. These two peak frequencies are also observed in the wake frequency plot of figure 3(h), $f_{vs}^* \approx 1$ and $f_{vs}^* \approx 4$. This higher frequency was also observed in figure 5(l), but mainly in the middle of the beam, and at this reduced velocity, it is distributed

along the length of the beam. This higher frequency is the result of shedding of vortices synchronised with the frequency of torsional oscillations – a torsional VIV response at this reduced velocity. We will discuss this behaviour with more details in §5.1. The sample time history and FFT plots of figure 6(*i,j*) show the low-frequency response and the relatively wide spectrum frequency content, although concentrated at approximately $f_{CF}^* = 1$. The co-existence of the two frequencies in the response is also seen in the vorticity plot of figure 8(*e*), where high-frequency vortices are shed at an angle with respect to the incoming flow. Figure 8(*f*) shows a few time steps later when the structure is at the other extreme CF displacement and the angle at which vortices are shed is switched from the previous case. This angle is the result of the translational galloping of the structure in the CF direction, while the shedding of vortices is synchronised with the torsional VIV of the structure. We will focus on the galloping behaviour of the prism at these high reduced velocities in the following section.

5. Galloping behaviour at high reduced velocities

5.1. Torsional galloping followed by torsional VIV

Galloping is observed at larger reduced velocities considered here. As seen in figure 4(*c*), torsional galloping starts at $U^* \approx 8$, followed by translational galloping at higher reduced velocities. Here, we focus on this behaviour by considering a combination of the CF, IL and torsional responses of the prism at these higher reduced velocities. Samples of time histories for the torsional displacement of the structure are given in the first row of figure 10, together with the FFTs of the response at these sample reduced velocities along the length of the prism in the second row of the figure. In the range where torsional galloping is observed ($8 < U^* < 10$), the torsional response occurs at a lower frequency of $f_{\theta}^* \approx 1$. This is also shown in the FFT plots of figure 11. At higher reduced velocities, where translational galloping occurs, the torsional oscillations are at a higher frequency of $f_{\theta}^* \approx 4$. When translational galloping is observed, the frequency of oscillations in the CF direction drops as the CF response switches from CF VIV to CF galloping. This is the opposite of what is observed in the torsional direction. In fact, the high-frequency oscillations as well as the high-frequency shedding that is observed at higher reduced velocities (for example, $U^* = 13.6$ in the sample cases that we have already discussed) are the results of synchronisation between the torsional oscillations of the prism with the shedding of vortices in the wake, while the prism also undergoes low-frequency CF galloping oscillations. The deflected wake in the vorticity plots of figure 8(*e,f*) shows these two frequencies: the high-frequency shedding as a result of the torsional VIV and low-frequency oscillations that show up in the form of deflected wake due to the galloping of the prism in the CF direction (and therefore the low-frequency oscillations in that direction). The synchronisation between the torsional oscillations and vortex shedding is also observed in the wake as synchronised vortices that are shed along the length of the prism, as shown in figure 12(*a*). When CF galloping dominates the response, the wake loses its synchronisation along the length of the prism, as shown in figure 12(*b*).

Based on these observations, one can summarise the galloping behaviour of the prism at these higher reduced velocities as follows. Initially, torsional galloping starts at approximately $U^* = 8$. This is accompanied by CF VIV in the third and fourth structural modes. At higher reduced velocities, the torsional galloping is replaced by torsional VIV (the vortex shedding is synchronised with the frequency of torsional oscillations) and CF VIV is replaced by CF galloping (which shows up as a mainly first-mode structural response of the prism).

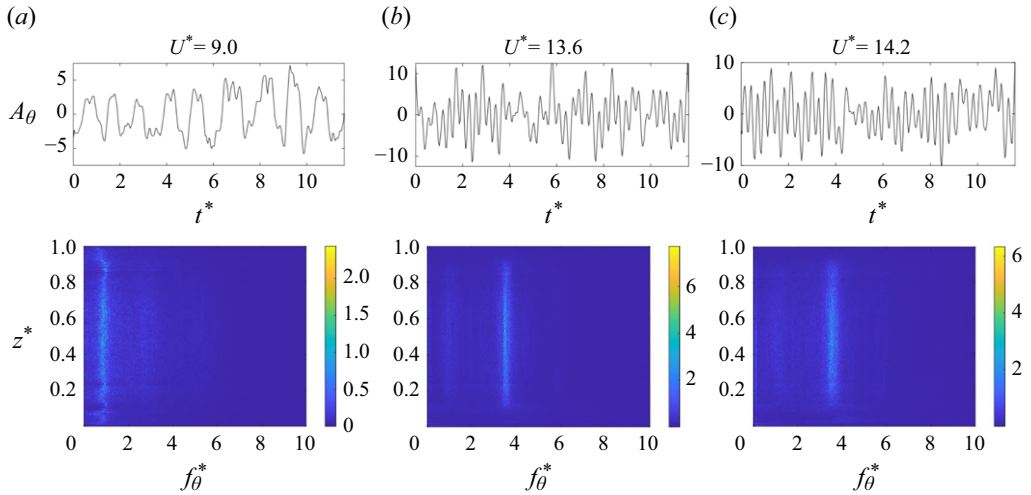


Figure 10. Time histories of the torsional response of the square prism at $z^* = 0.5$ (upper row) together with the frequency contents of the torsional response along the length of the prism (lower row) at (a) $U^* = 9.0$, (b) $U^* = 13.6$ and (c) $U^* = 14.2$, where torsional ($U^* = 9.0$) and translation ($U^* = 13.6$ and 14.2) galloping responses are observed.

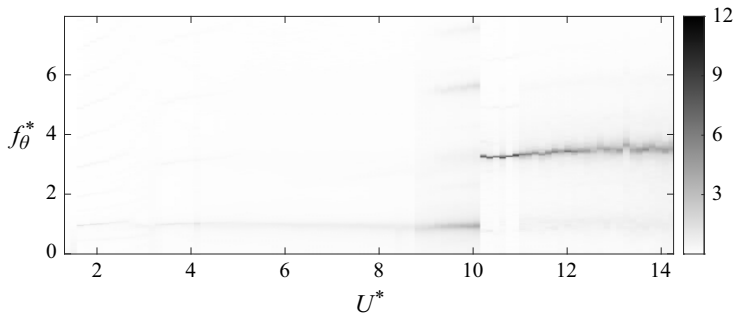


Figure 11. Normalised frequency of torsional oscillations versus reduced velocity at $z^* = 0.5$.

5.2. Prism trajectories at higher reduced velocities

When galloping (torsional as well as translational) is observed in the response of the system, the IL oscillations exhibit large amplitudes. This is clearly observed in the plots of CF versus IL oscillations at different locations along the length of the structure for larger reduced velocities shown in figure 13. The large-amplitude CF oscillations are accompanied by large IL oscillations at amplitudes comparable with the CF amplitude. This is observed for the case of $U^* = 9.0$ for the first time, where torsional galloping is observed. The occurrence of torsional galloping leads to large-amplitude oscillations in both the CF and IL displacements as well. The trajectories at this reduced velocity are mainly crescent like and are bent away from the incoming flow (note that the mean values of displacements are removed from these plots). For the case of $U^* = 10.1$ where we observe a mainly fourth-mode VIV response, both the CF and IL amplitudes drop significantly. Then, for $U^* = 13.6$ and 14.2 , where CF galloping is observed, large-amplitude figure-eight trajectories are observed along the length of the prism again.

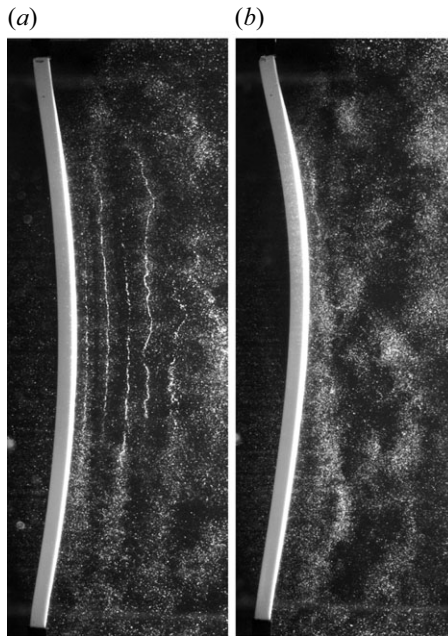


Figure 12. Wake of the square prism along its length as the structure undergoes galloping at $U^* = 13.6$ during two different time periods of oscillations. The snapshot in (a) corresponds to a time when torsional VIV is dominant and the snapshot in (b) corresponds to a time when CF galloping is dominant.

Particularly, the trajectories at $z^* = 1/2$ exhibit the maximum amplitudes that are observed in the first-mode CF galloping response. These trajectories are shown again in [figure 14](#) for one single cycle of oscillations together with the orientation of the prism cross-section to give an overall view of the CF, IL and torsional response of the prism.

For the cases shown in the plot, the direction that the prism follows on the figure-eight trajectories is different for the two U^* values. For $U^* = 13.6$, the prism follows a clockwise (CW) figure-eight (in which case, at its two extreme CF locations, the prism moves in the direction of the incoming flow – noted by an arrow in the figure), while for $U^* = 14.2$, it follows a counterclockwise (CCW) trajectory. Previous observations of the VIV response of 2DOF systems (Dahl *et al.* 2010; Carlson *et al.* 2021) and flexible cylinders (Bourguet *et al.* 2011a) have shown that when energy is transferred from the flow to the structure, the structure follows a CCW trajectory. In regions where the flow damps the response of the cylinder, these previous studies have shown that either CW or CCW trajectories could be observed. In the trajectories shown here, the response contains both VIV and galloping. In [figure 15](#), we plot these responses as two separate trajectories: one corresponding to a pure low-frequency CF galloping response, where we remove the high-frequency response, and one corresponding to a pure high-mode VIV response, where we remove the low-frequency response. We do this for two ranges of the prism response. One corresponding to a clear figure-eight response, and one corresponding to a range where the total response is of smaller amplitude and follows a rather complicated trajectory. The results show that in both cases, the galloping trajectory follows the same direction as the total trajectory, while the trajectory in the VIV-dominated response, when a figure-eight trajectory is observed (note that in the high frequency response of case (b), no visible figure-eight trajectory is observed), follows a CCW figure-eight, independent from the direction that the total trajectory of the prism followed.

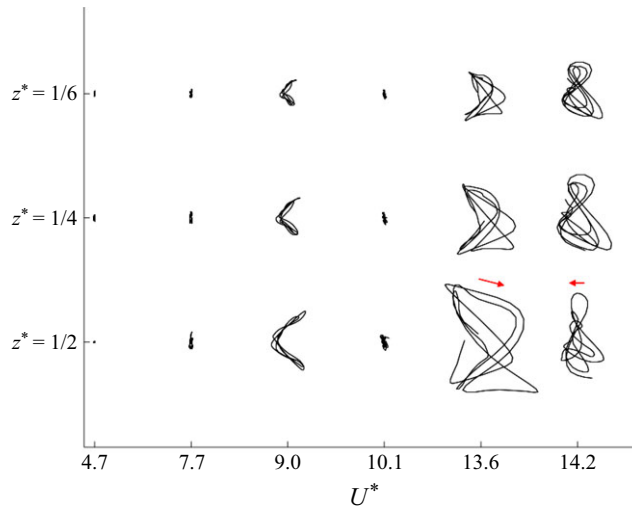


Figure 13. CF versus IL trajectories of the prism at $z^* = 1/6, 1/4$ and $1/2$ along its length and at sample U^* values. The three cases with large CF and IL amplitudes are the cases that correspond to the galloping-dominated response of the prism: $U^* = 9.0, 13.6$ and 14.2 . The other cases correspond to the VIV-dominated response at the second mode ($U^* = 4.7$), third mode ($U^* = 7.7$) and fourth mode ($U^* = 10.1$).

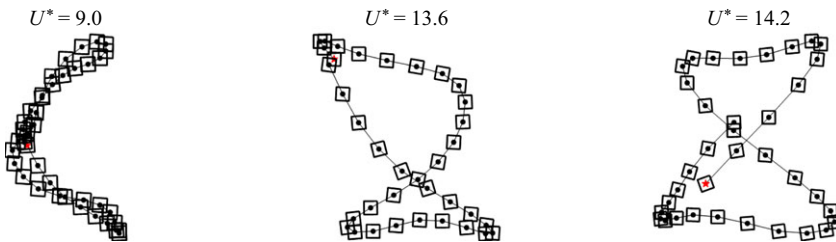


Figure 14. CF versus IL trajectories of the sample cases with galloping response together with the orientation of the prism cross-section, over one cycle of oscillations. The earliest square shown is marked with a red star. Cross-section dimensions are reduced relative to the trajectory for clarity.

6. On the increase in tension by increasing the flow velocity

In the tests discussed here, the reduced velocity is increased by increasing the flow velocity. As the flow velocity is increased, the prism experiences increasing mean drag forces, causing a growing mean deflection of the prism in the downstream direction. As the prism is deflected, the tension and the length of the structure both increase, which could lead to a variation in the natural frequency, as in a tension-dominated structure, the natural frequency is proportional to the square root of the tension and inversely proportional to the length, i.e. $f_n \propto \sqrt{T}/L$. To quantify this variation in the natural frequency in the tests conducted here, we calculated the mean elongation from the tracked displacement data in the inline direction. We independently measured the ratio between the axial extension of the prism and the induced tension, and found a ratio of 0.06 N mm^{-1} between the induced tension and increase in length. Using this ratio and the measured mean elongation of the structure, we calculated the induced tension on the structure at each reduced velocity. In figure 16, we plot the ratio of this reduced-velocity-specific natural frequency, f_{nw,U^*} , to the original natural frequency in water with the original length of the prism, f_{nw} , to

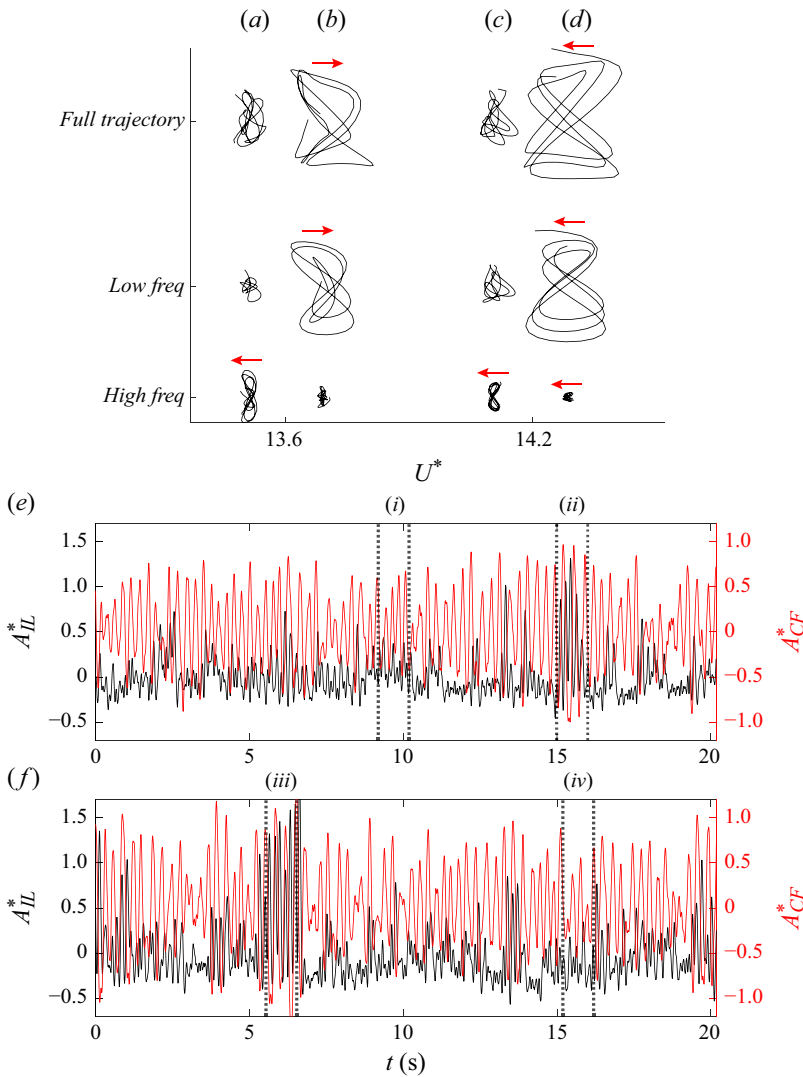


Figure 15. Sample trajectories for two different reduced velocities: (a,b) $U^* = 13.6$ and (c,d) $U^* = 14.2$. For each reduced velocity, two portions of the time history are shown: one with mainly low-amplitude response (a,c), and one with mainly large-amplitude response (b,d). Low-frequency and high-frequency filtered signals are shown in the lower rows. The IL response was filtered at twice the frequency that the CF response was filtered. Where there is a discernible figure-eight trajectory, arrows show the direction of prism motion on each trajectory. The longer time histories for both reduced velocities are shown (e) for $U^* = 13.6$ and (f) for $U^* = 14.2$, with the parts shown in the trajectories highlighted in the time histories. Trajectory (a) corresponds to section (i) of the time history, (b) to (ii), (c) to (iv) and (d) to (iii).

quantify the increase in natural frequency versus reduced velocity due to static bending of the prism. To confirm these results, we did an independent test in which we attached an ATI Industrial Automation Nano 17 6-axis force sensor to one end of the prism, and stretched the prism to the maximum increased length that we had observed in its flow-induced responses and measured the induced tension to be 1.3 N, i.e. 30 % larger than the original tension applied to the unstretched prism. We then placed the prism in otherwise still water and conducted a decay test to measure the natural frequency in water that

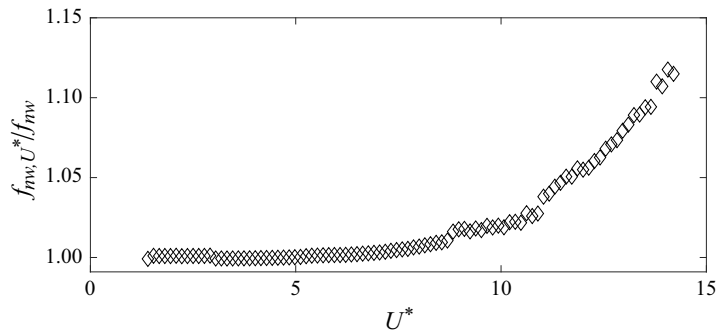


Figure 16. Ratio between the reduced-velocity-specific natural frequency in water due to the bending of the flexible prism, f_{nw,U^*} , and the natural frequency in water with the original length of the beam, f_{nw} , versus reduced velocity.

corresponds to this stretched case. We used this information and calculated the natural frequency in water in this configuration to be 4.5 Hz, approximately 15 % larger than the values measured in the unstretched case. This value of $f_{nw,U^*}/f_{nw}$ is very close to the maximum value we calculated using our first method and shown in figure 16. These results confirm that the increased bending does not affect the natural frequency within the range of reduced velocities where CF VIV is observed, as the ratio stays close to one. There is a slight influence of static bending on the response within the galloping range, as we observe an increase in the reduced-velocity-specific natural frequency in this range, which reaches approximately 12 % of the original natural frequency at the maximum reduced velocity tested here.

7. Conclusions

We discuss a series of experiments on the flow-induced response of a flexible square prism under tension placed perpendicular to the flow of water such that the flat side of the structure sees the flow first. The square prism was made of silicone rubber, and had a mass ratio of $m^* = 1.23$ and an aspect ratio of $L/D = 36.2$. In our experiments, we increased the flow velocity in small increments and covered a reduced velocities range of $1.4 < U^* < 14.2$, corresponding to a Reynolds number range of $500 < Re < 5100$. At each flow velocity, we measured the prism's displacements in the CF and IL directions using two high-speed cameras that synchronously recorded the response of the prism from two perpendicular sides. Then we tracked the motion of each pixel at the edges along the entire length of the structure to obtain a highly detailed displacement measurement along the structure's length, and then calculated the torsion values using these displacement measurements. At each flow velocity, in addition to displacement measurements, we conducted flow visualisations in the wake to both quantify the frequency of shedding of vortices in the wake and observe the wake behaviour as the prism went through different modes of oscillations.

We show that the prism goes through a series of VIV responses initially as the flow velocity is increased. Synchronisations between the shedding frequency and oscillation frequency occur at the first, second and third modes of the structure resulting in the structure's response in those respective modes. The switching from one mode to another occurs rather abruptly without regions of simultaneous excitations of two modes. For the range of reduced velocities where mainly first, second and third mode VIV responses are observed, the displacements in the IL and torsional directions are negligible. At higher

reduced velocities and towards the end of the range where the third-mode CF VIV is observed, we observe a linear increase in the torsional displacement with increasing reduced velocity for a range of reduced velocities – a torsional galloping response. This torsional galloping response results in increased amplitudes of oscillations in the CF and IL directions, and relatively large-amplitude crescent-like trajectories of the prism with comparable IL and CF amplitudes. At slightly larger reduced velocities, the torsional amplitude reaches a plateau at approximately 15° , the CF VIV response switches to a mainly fourth-mode response and signs of CF galloping response appear. This is then followed by a mainly first-mode and large-amplitude galloping response in the CF direction, which is accompanied by IL oscillations with a comparable amplitude and at a frequency twice the CF oscillations, which results in large-amplitude figure-eight trajectories. The torsional response in this range stays at a relatively constant amplitude, but jumps to a much higher frequency compared with the frequency of torsional galloping that was observed earlier. These higher frequency torsional oscillations are synchronised with the frequency of vortices that are shed in the wake of the prism in this range of reduced velocities. This range of reduced velocities, therefore, corresponds to a combined CF galloping and torsional VIV. By taking a closer look at the VIV and galloping responses that co-exist at these higher reduced velocities, we observe that when the full trajectory follows a figure-eight shape, the galloping-dominated trajectory follows the same direction as the total trajectory; however, the trajectory in the VIV-dominated response moves in the CCW direction.

Overall, in the CF response, we observe VIV, in successively increasing structural modes, followed by galloping in the first mode. In the torsional response, we observe galloping first and VIV at higher reduced velocities. The torsional responses stay in the first torsional mode for both VIV and galloping cases. This behaviour results in the co-existence of torsional galloping and CF VIV over a range of lower reduced velocities, and CF translational galloping and torsional VIV at higher reduced velocities. The transition from low-mode excitation to high-mode excitation by increasing reduced velocity is generic in VIV of flexible structures and has been observed before especially for cases with circular cross-sections. The observed transition to transverse galloping at higher reduced velocities, and the co-existence of the transverse VIV and torsional galloping as well as transverse galloping and torsional VIV are the main novel observations in the present work.

In the system considered here, the torsional natural frequency was larger than the third-mode natural frequency in the CF direction. If the torsional natural frequency were smaller, let us say, smaller than the third-mode natural frequency in the CF direction, then the transition to torsional VIV could have been expected to occur at lower reduced velocities. The sequence of excitation of increasingly higher CF modes with increasing reduced velocity and then transitioning to torsional VIV, however, would not have been changed. In flexible beams, the first-mode natural frequency in the CF direction is normally smaller than the first torsional natural frequency, which means that synchronisation with the shedding frequency would be expected to start in the CF direction, and then at higher reduced velocities, transition to the torsional direction. The number of CF modes that would have been excited before the start of torsional VIV would have been a function of the ratio between the torsional natural frequency and the first CF natural frequency.

Declaration of interests. The authors report no conflict of interest.

REFERENCES

- BLEVINS, R. D. 1990 *Flow-Induced Vibration*. Krieger.
BOURGUET, R., KARNIADAKIS, G.E. & TRIANTAFYLLOU, M.S. 2011a Vortex-induced vibrations of a long flexible cylinder in shear flow. *J. Fluid Mech.* **677**, 342–382.

- BOURGUET, R., MODARRES-SADEGHI, Y., KARNIADAKIS, G.E. & TRIANTAFYLLOU, M.S. 2011b Wake-body resonance of long flexible structures is dominated by counterclockwise orbits. *Phys. Rev. Lett.* **107** (13), 134502.
- CAGNEY, N. & BALABANI, S. 2014 Streamwise vortex-induced vibrations of cylinders with one and two degrees of freedom. *J. Fluid Mech.* **758**, 702–727.
- CARLSON, D., CURRIER, T. & MODARRES-SADEGHI, Y. 2021 Flow-induced vibrations of a square prism free to oscillate in the crossflow and inline directions. *J. Fluid Mech.* **919**, A2.
- CHAPLIN, J., BEARMAN, P., HUARTE, F. & PATTENDEN, R. 2005 Laboratory measurements of vortex-induced vibrations of a vertical tension riser in a stepped current. *J. Fluids Struct.* **21** (1), 3–24.
- CURRIER, T.M., CARLETON, A.G. & MODARRES-SADEGHI, Y. 2021 Dynamics of a hydrofoil free to oscillate in the wake of a fixed, constantly rotating or periodically rotating cylinder. *J. Fluid Mech.* **923**, A21.
- DAHL, J., HOVER, F. & TRIANTAFYLLOU, M. 2006 Two-degree-of-freedom vortex-induced vibrations using a force assisted apparatus. *J. Fluids Struct.* **22** (6-7), 807–818.
- DAHL, J., HOVER, F., TRIANTAFYLLOU, M., DONG, S. & KARNIADAKIS, G. 2007 Resonant vibrations of bluff bodies cause multivortex shedding and high frequency forces. *Phys. Rev. Lett.* **99** (14), 144503.
- DAHL, J., HOVER, F., TRIANTAFYLLOU, M. & OAKLEY, O. 2010 Dual resonance in vortex-induced vibrations at subcritical and supercritical Reynolds numbers. *J. Fluid Mech.* **643** (1), 395–424.
- GURIAN, T., CURRIER, T. & MODARRES-SADEGHI, Y. 2019 Flow force measurements and the wake transition in purely inline vortex-induced vibration of a circular cylinder. *Phys. Rev. Fluids* **4** (3), 034701.
- HUERA-HUARTE, F. 2024 Vortex-induced vibration of flexible cylinders in cross-flow. *Annu. Rev. Fluid Mech.* **57**, 285–310.
- HUERA-HUARTE, F. & BEARMAN, P. 2009 Wake structures and vortex-induced vibrations of a long flexible cylinder-part I: dynamic response. *J. Fluid. Struct.* **25** (6), 969–990.
- JAUVTIS, N. & WILLIAMSON, C. 2004 The effect of two degrees of freedom on vortex-induced vibration at low mass and damping. *J. Fluid Mech.* **509** (6), 23–62.
- MA, L., LIN, K., FAN, D., WANG, J. & TRIANTAFYLLOU, M.S. 2022 Flexible cylinder flow-induced vibration. *Phys. Fluids* **34** (1), 011302.
- MODARRES-SADEGHI, Y. 2022 *Introduction to Fluid-Structure Interactions*. Springer.
- NEMES, A., ZHAO, J., LO JACONO, D. & SHERIDAN, J. 2012 The interaction between flow-induced vibration mechanisms of a square cylinder with varying angles of attack. *J. Fluid Mech.* **710**, 102–130.
- PAÏDOUSSIS, M.P., PRICE, S.J. & DE LANGRE, E. 2010 *Fluid-Structure Interactions: Cross-Flow-Induced Instabilities*. Cambridge University Press.
- SARPKAYA, T. 2004 A critical review of the intrinsic nature of vortex-induced vibrations. *J. Fluids Struct.* **19** (4), 389–447.
- SEYED-AGHAZADEH, B., BENNER, B., GJOKOLLARI, X. & MODARRES-SADEGHI, Y. 2021 An experimental investigation of vortex-induced vibration of a curved flexible cylinder. *J. Fluid Mech.* **927**, A21.
- SEYED-AGHAZADEH, B., CARLSON, D. & MODARRES-SADEGHI, Y. 2017 Vortex-induced vibration and galloping of prisms with triangular cross-sections. *J. Fluid Mech.* **817**, 590–618.
- SEYED-AGHAZADEH, B., EDRAKI, M. & MODARRES-SADEGHI, Y. 2019 Effects of boundary conditions on vortex-induced vibration of a fully submerged flexible cylinder. *Exp. Fluids* **60** (3), 38.
- SEYED-AGHAZADEH, B. & MODARRES-SADEGHI, Y. 2016 Reconstructing the vortex-induced-vibration response of flexible cylinders using limited localized measurement points. *J. Fluid. Struct.* **65**, 433–446.
- STAMHUIS, E. & THIELICKE, W. 2014 Pivlab—towards user-friendly, affordable and accurate digital particle image velocimetry in MATLAB. *J. Open Res. Softw.* **2** (1), 30.
- TRIM, A., BRAATEN, H., LIE, H. & TOGNARELLI, M. 2005 Experimental investigation of vortex-induced vibration of long marine risers. *J. Fluid. Struct.* **21** (3), 335–361.
- WILLIAMSON, C. & GOVARDHAN, R. 2004 Vortex-induced vibrations. *Annu. Rev. Fluid Mech.* **36** (1), 413–455.
- WU, X., GE, F. & HONG, Y. 2012 A review of recent studies on vortex-induced vibrations of long slender cylinders. *J. Fluid. Struct.* **28**, 292–308.
- ZHAO, J., LEONTINI, J., LO JACONO, D. & SHERIDAN, J. 2014 Fluid–structure interaction of a square cylinder at different angles of attack. *J. Fluid Mech.* **747**, 688–721.
- ZHAO, J., NEMES, A., JACONO, D. & SHERIDAN, J. 2010 The effect of incidence angle variation of a square cylinder on its dynamic response and wake states. In *Proceedings of the 17th Australasian Fluid Mechanics Conference, AFMC Auckland*, pp. 1–4.